



OPEN

Pressure driven polymorphic transitions in nanocrystalline Lu_2O_3 , Tm_2O_3 and Eu_2O_3

Neha Bura^{1,2}, Ankit Bhoriya^{1,2}, Deepa Yadav^{1,2}, Srihari Velaga³, Bal Govind^{1,2}, Jasveer Singh¹, Himanshu Kumar Poswal³ & Nita Dilawar Sharma^{1,2}✉

The crystallite size of the materials considerably influences the material properties, including their compressibility and resistance to external forces and the stability of the crystalline structure; a corresponding study for which, so far, has been limited for the important class of nanocrystalline Rare Earth Sesquioxides (REOs). In the present study, we report the crystallographic structural transitions in nanocrystalline Rare Earth Oxides (REOs) under the influence of pressure, investigated via high-energy X-Ray Diffraction (XRD) measurements. The study has been carried out on three of the REOs, namely Lutetium oxide (Lu_2O_3), Thulium oxide (Tm_2O_3) and Europium oxide (Eu_2O_3) up to the pressures of 33, 22 and 11 GPa, respectively. The diffraction data of Lu_2O_3 and Tm_2O_3 suggests the occurrence of irreversible structural transitions from cubic to monoclinic phase, while Eu_2O_3 showed a transition from the cubic to hexagonal phase. The transitions were found to be accompanied by a collapse in the volume and the resulting Pressure–Volume (P–V) graphs are fitted with the 3rd order Birch–Murnaghan (BM) equation of state (EOS) to estimate the bulk moduli and their pressure derivatives. Our study establishes a qualitative relationship between the crystallite size and various material properties such as the lattice parameters, transition pressure, bulk modulus etc., and strengthens the knowledge regarding the behaviour of this technologically important class of materials.

Rare earth sesquioxides (REOs) have been an interesting area of study in past years due to their versatile technological and scientific significance. They have various applications in every field of science and find applications as coating materials to stabilize high voltage lithium layered oxide cathodes¹, as well as in environmental barrier coatings². They are also used as a doping materials in metal oxides to increase their photocatalytic activity³, blended with various polymers to increase their gamma shielding capacity⁴. These materials are of strategic importance and find applications in solid oxide fuel cells⁵, nuclear security applications⁶, neutron absorbers⁷, laser crystals^{8,9}, nuclear waste host materials¹⁰, chemical machine polishing^{11,12}, light emitting devices¹³, rare earth magnets, control rods for fast breeder reactors¹⁴, radiation shielding^{10,15,16}, and catalysis¹⁷ etc. REO nanoparticles are also used for biomedical and dental applications^{18–20}. Due to these numerous applications in all fields of science, it becomes necessary to study the behavior of these materials under varying conditions.

Three polymorphic forms viz. cubic, monoclinic and hexagonal are usually exhibited by REOs. They exhibit these structures depending on their cationic radii. As we move from La to Lu in the periodic table, the cationic radii decrease and their atomic masses increase. Heavier sesquioxides exhibit cubic structure (C-type) having a space group $Ia-3$ (206) and $Z=16$ while the lighter ones are found to be in a hexagonal phase (A-type) with space group $P-3m1$ and $Z=1$. The medium cations i.e., Sm to Gd can exist in the monoclinic phase (B-type) having a space group $C2/m$ and $Z=6$. Furthermore, it is known that under the application of external forces, the materials undergo phase transitions as they try to adjust their structure to minimize the lattice energy and achieve equilibrium. The structural transition from cubic to monoclinic to hexagonal is accompanied by volume collapse. The hexagonal phase is known to have the least volume among all three phases. However, the volume change in the case of the transition from the cubic to monoclinic phase has a high value, and contrary to this, the transition from the monoclinic to hexagonal phase is accompanied by small changes in the volume²¹.

The structural transition studies in the REOs are an interesting area of research and a number of researchers have been working on the same. Jiang et al. studied the high-pressure behavior of the Eu_2O_3 using Angle

¹CSIR- National Physical Laboratory, Dr. K. S. Krishnan Marg, New Delhi 110012, India. ²Academy of Scientific and Innovative Research (AcSIR), Ghaziabad 201002, India. ³High Pressure and Synchrotron Radiation Physics Division, Physics Group, HBNI, Bhabha Atomic Research Centre, Mumbai 400085, India. ✉email: ndilawar@nplindia.org

Dispersive X-Ray Diffraction (ADXRD) and observed a cubic to hexagonal transition with a volume collapse of 9.6 %²². Yu et al. reported a phase transition from cubic to hexagonal in nano-Eu₂O₃ which starts at 9.3 GPa²³. Our group also reported a phase transition from cubic to monoclinic in Eu_{1-x}O₃ having some content of the Eu_{1-x}O₃²⁴. Recently, we have also reported a cubic to hexagonal transition in pure Eu₂O₃ which initiated at 4.79 GPa and completed at 15 GPa²⁵. The pure Eu₂O₃ shows a direct transition from the cubic to the hexagonal phase. Moreover, Lu₂O₃ and Tm₂O₃ have been reported to show transition from cubic to monoclinic phase. Sahu et al. reported a transition from the cubic to monoclinic phase in Tm₂O₃ at 7 GPa using the XRD studies²⁶. A phase transition from cubic to monoclinic phase at 12 GPa has been reported by Irshad et al. using Raman as well as XRD measurements in Tm₂O₃²⁷. A cubic to monoclinic phase transition in Lu₂O₃, which started at a pressure of 12.7 GPa and completed at 18.2 GPa has been reported by Jiang et al.²⁸. Lin et al. observed that a cubic to monoclinic transition started at a pressure of 17 GPa in Lu₂O₃²⁹. Our group has also studied the pressure behavior of Lu₂O₃ using Raman spectroscopy and found that the cubic phase is stable up to the pressure of 15.6 GPa³⁰. However, there are discrepancies in the value of the transition pressures reported so far.

Further, nanocrystalline materials, owing to their nanometric size, have fascinating properties different than the bulk materials due to the large surface area and large surface to volume ratio. These aspects of the nanomaterials also affect the crystallographic transition pressures of the materials. In general, the transition pressure of the REO nanomaterials is found to be higher than their bulk counterpart^{23,31}. Such a study has also been reported for CeO₂³². From the mechanical point of view, this could be attributed to the Hall–Petch effect due to which, the grain boundaries in the material affect its yield strength and with the decreasing grain size the yield and flow stress required for continuous plastic deformations increase. However, targeted investigations of pressure driven transitions in nanocrystalline REOs still have much scope.

In this study, we present the pressure-driven structural changes investigated via variation in the diffraction peaks for three of the nanocrystalline REOs namely Eu₂O₃, Tm₂O₃ and Lu₂O₃ using the high-pressure XRD (HPXRD) study up to the pressures of 11 GPa, 22 GPa, and 33 GPa respectively. We discuss the influence of the crystallite size on various material properties such as bulk modulus, phase transitions pressure, etc., and attempt to establish a qualitative relation between them, which has been missing so far. Along with this, we also report the dependency of the lattice parameters on pressure.

Experimental procedure

The REOs of purity 99.99% were used as the starting materials. The powder sample of the Lu₂O₃ was procured from Johnson Matthey, UK and powder samples of Tm₂O₃ and Eu₂O₃ were procured from Alfa Aesar respectively.

The HPXRD measurements were carried out on beamline 11 of Indus 2 synchrotron radiation facility at RRCAT, Indore, India. To carry out the measurements, Lu₂O₃ and Tm₂O₃ were loaded in Fe-gaskets with a hole size of about 80 μm along with a few ruby chips which were used as pressure calibrators. However, for Eu₂O₃, the Fe-gasket was used with the gold as a pressure calibrator. In all the HPXRD studies, a mixture of methanol and ethanol in a ratio of 4:1 was used as the pressure-transmitting medium. The hydrostatic limit for this pressure transmitting medium is 10.5 GPa³³. The wavelength of the incident radiation was tuned at 0.696112 Å for both Lu₂O₃ and Tm₂O₃, and tuned at 0.634857 Å for the Eu₂O₃. The distance and orientation of the detector were calibrated using CeO₂ powder as well as LaB₆.

Characterization at ambient

All the samples, in their ambient phase, were found to exhibit the cubic crystalline phase with space group *Ia-3(206)*. The various characterization studies including XRD, Raman spectroscopy, SEM and EDX measurements, carried out on these samples have been reported elsewhere in references^{25,30,34}. The obtained diffraction patterns of the sesquioxides were compared with the JCPDS data cards, #430121 for Lu₂O₃, # 431034 for Tm₂O₃ and #340392 for Eu₂O₃. The crystallite size of all three materials, estimated using Williamson-Hall plot, was found to be in the range of 30–66 nm which confirmed the nanocrystalline nature of all the studied materials as mentioned in Table 1. The phase purity of the samples was also further confirmed by Rietveld analysis of the ambient XRD spectra of the REOs obtained using the synchrotron radiation source as shown in Fig. S1. The various lattice parameters and ambient unit cell volumes obtained from the refinement are also shown in Table 1.

Pressure-dependent XRD measurements and data analysis

Lutetium oxide (Lu₂O₃)

For Lu₂O₃, the pressure-dependent measurement was carried out up to a pressure of 33 GPa. Figure 1 shows the pressure-dependent XRD results. The XRD pattern at any given pressure contains the peak of the sample in

Material	Lattice parameters (Å)			Unit cell volume (Å ³)	Volume/Z (Å ³)	Crystallite Size ^{25,34}
	a	b	c			
Eu ₂ O ₃	10.8540 (2)			1278.71 (4)	79.92	66 nm
Tm ₂ O ₃	10.4723 (3)			1148.48 (5)	71.78	35 nm
Lu ₂ O ₃	10.3755 (1)			1116.92 (3)	69.81	30 nm

Table 1. Lattice parameters and unit cell volume of the REOs.

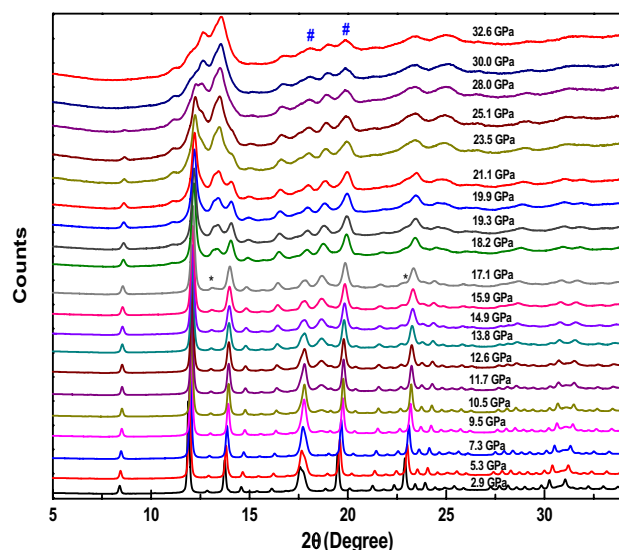


Figure 1. XRD patterns of Lu_2O_3 with increasing pressures. Each diffraction data is marked with the corresponding pressure and the peaks corresponding to the gasket material have been marked with #.

question, as well as the peaks corresponding to the gasket material (Fe). As we increase the pressure, the peaks of the cubic phase start shifting towards the higher values of 2θ while simultaneously, peaks also start to broaden. Up to a pressure of 17.1 GPa, peaks only shift towards the higher 2θ side. However, at around 17.1 GPa new peaks started to develop at about $2\theta = 13.45^\circ$, which is marked with * in Fig. 1. In addition, a weak shoulder to the cubic phase peak at $2\theta = 22.96^\circ$ also begins to develop. With further increasing pressure, the intensity of these peaks increases significantly at the expense of the intensity of the cubic phase peaks.

At around 30 GPa, the peaks corresponding to the cubic phase disappear entirely. The newly developed peaks agree very well with the monoclinic phase of the material which is confirmed by Rietveld refinement of the high-pressure data. Hence, we can say that a pressure-driven structural transition from the cubic to the monoclinic phase has been observed. This phase transition starts at 17.1 GPa of pressure and completes at 30 GPa. Beyond 30 GPa, the monoclinic phase of the material is found to be stable till the highest studied pressure i.e., 32.6 GPa.

Thulium oxide (Tm_2O_3)

The pressure-driven changes can be seen in Tm_2O_3 up to the highest studied pressure of around 22 GPa in Fig. 2. Along with the peaks of the cubic phase of the sample, the peaks corresponding to the Fe have also been observed in the diffraction pattern. The cubic phase of the material is found to be stable till the pressure of 12.8 GPa. At a pressure of 14.0 GPa, new peaks started appearing in the diffraction pattern at 2θ values of 13.04° and 22.57° . Similar to the observation in Lu_2O_3 , with increasing pressures, the intensity of these peaks is found to be increasing while the intensity of the cubic phase peaks decreases. These new peaks also agree very well with the peaks of the monoclinic phase as concluded by Rietveld refinement of the data. However, till the highest studied pressure the transition was not completed since the peak corresponding to the Miller indices (222) belonging to the cubic phase, can still be observed in the diffraction pattern marked by \$ in Fig. 2.

Europium oxide (Eu_2O_3)

The structural changes in Eu_2O_3 with increasing applied pressure are shown in Fig. 3. With increasing pressure, the peaks were again observed to be shifted towards the higher values of 2θ , and simultaneously, the broadening of the peaks has been observed. Till the pressure of 4.0 GPa, we have only observed the broadening and shifting of the peaks. Nevertheless, at a pressure of 7.4 GPa, a new peak has been observed at $2\theta = 12.7^\circ$, which is found to belong to the hexagonal phase of the sample, as confirmed by Rietveld refinement. With further increasing pressure, the intensity of this peak increases along with the emergence of additional new peaks. On the other hand, peaks corresponding to the cubic phase of the sample are losing their intensity, confirming the formation of a new phase at the cost of the current phase. However, till the highest studied pressure, the peaks corresponding to the cubic as well as hexagonal phases have been observed. Hence it is clear that up to a pressure of 11 GPa, the transition has not been completed.

Data analysis

As mentioned, the Rietveld refinements at all the pressure points have been carried out for all the three samples using the CIF files available at Crystallographic Open Database (COD). For the refinement of the data, pseudo-Voigt peak shape has been used in the FullProf software. Rietveld refinement for all of three oxides at three selected pressure points is shown in Fig. 4. The values of the chi-square have been mentioned in the graphs which

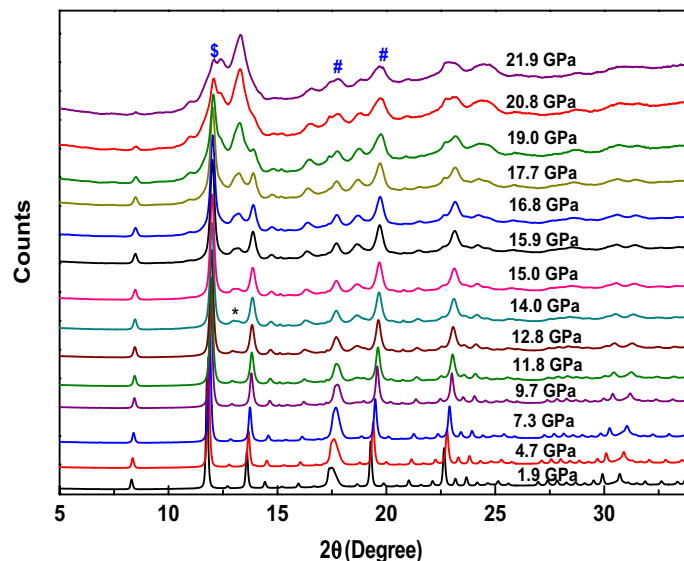


Figure 2. Evolution of the diffraction pattern of Tm_2O_3 with increasing applied pressure. Peaks of the gasket material, i.e., Fe are marked with #.

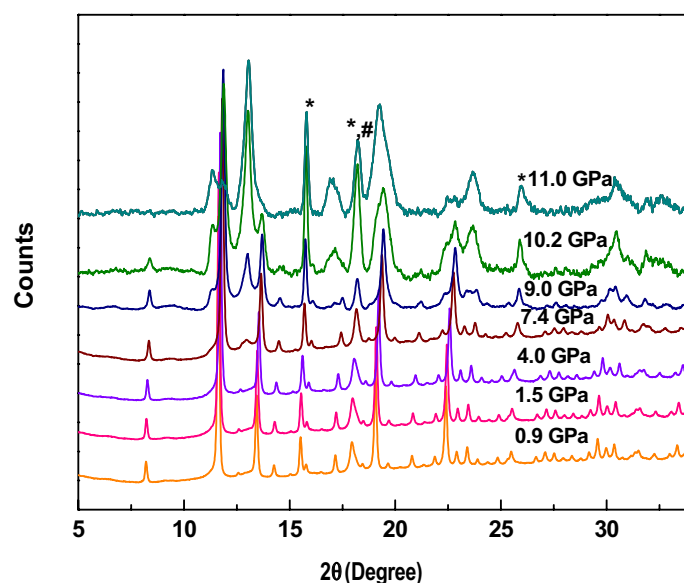


Figure 3. Pressure-driven changes in the diffraction pattern of Eu_2O_3 . The peaks corresponding to Au (Pressure calibrator) and Fe (gasket material) have been marked with * and # respectively.

decides the goodness of the refinement. The values of the lattice parameters and volumes have been estimated using the refinement data.

The applied pressure affects the intermolecular bonding in the materials and this compression results in the decrease in the volume. As expected, we have also observed this decrease in the volume for all the samples with applied pressure as shown in Fig. 5. The squares and circles show the experimentally obtained pressure-volume data. All the three samples show significant reduction in volume near the transition pressures.

This pressure volume data was fitted using the BM EOS. However, prior to EOS fitting, the data was deduced from the F-f plot (Fig. S2). F represents the normalized stress and f is Eulerian strain and the estimations were carried out using the equations

$$F = \frac{P}{3f(1+2f)^{2.5}}, \quad (1)$$

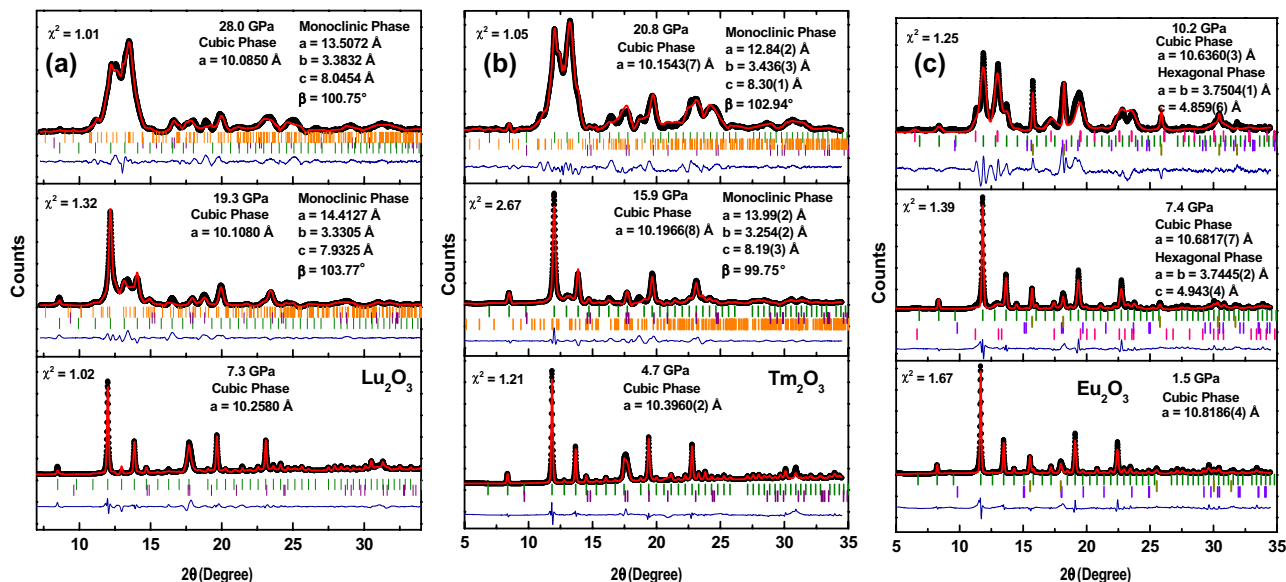


Figure 4. Rietveld refinement of (a) Lu_2O_3 and (b) Tm_2O_3 at a few applied pressures. The green and orange lines represent the Bragg's positions corresponding to cubic and monoclinic phases respectively. (c) Rietveld refined diffraction data for Eu_2O_3 at various applied pressures. Green and pink ticks represent the Bragg's positions corresponding to cubic and hexagonal phases of the Eu_2O_3 respectively. The dark yellow line represents the Bragg's position of the gold and violet line represents the Bragg's position of the Fe.

$$f = 0.5 \left[\left(\frac{V_0}{V} \right)^{2/3} - 1 \right]. \quad (2)$$

The F-f plot comes out to be a straight line (Fig. S2), and hence 3rd order BM EOS has been used for the fitting of the obtained P-V data, which is given by

$$P(V) = \frac{3B_0}{2} \left[\left(\frac{V_0}{V} \right)^{7/3} - \left(\frac{V_0}{V} \right)^{5/3} \right] \left\{ 1 + \frac{3}{4} (B_0' - 4) \left[\left(\frac{V_0}{V} \right)^{2/3} - 1 \right] \right\}. \quad (3)$$

In the above equation V_0 and V represent the unit cell volume of the material at ambient pressure and at pressure P respectively, B_0 is the bulk modulus of the elasticity and B_0' is its pressure derivative.

The solid lines in Fig. 5 show the fit obtained for the experimental variation of the volume with pressure. In case of Lu_2O_3 and Tm_2O_3 , the volume data is shown for the ambient cubic and the high-pressure monoclinic phase, while in case of Eu_2O_3 volume data is shown for the ambient cubic and the high-pressure hexagonal phase. From fitted data obtained using Eq. (3), the values of the bulk modulus and its pressure derivatives are estimated, which are given in Table 2 and mentioned in the graphs.

The table also compares the presently obtained values and the reported literature values and show a good agreement with the work of Irshad et al.^{27,35} for Tm_2O_3 and Eu_2O_3 .

Discussion

The predominance of surface atoms at the nanoscale, with their varied contributions to the cohesive energy through their related surface energies, can completely alter a phase energy landscape with a variety of effects. Due to this energy contribution, the phase diagram of the nanomaterial can change in comparison to its bulk counterpart in terms of the change in the transition pressures, involves new crystallographic structures or have amorphous states. In the present study, we have also observed a shift in the transition pressures in case of Lu_2O_3 and Tm_2O_3 towards higher value of pressure as compared to the reported studies^{27–29}. However, in the case of Eu_2O_3 , the transition pressure of 7.4 GPa, observed presently, is lower than the transition pressure reported by Jiang et al.²². Eu_2O_3 showed a transition to hexagonal phase while the other two samples progressed to monoclinic phase at high pressures.

The normal trend of the structural phase transitions in the REOs under the application of pressure is cubic to monoclinic and monoclinic to hexagonal^{36–39}. However, exceptions have been observed in a number of oxides which show a direct transition from cubic to hexagonal transition^{40–46}. This can be due to the lower energy of the hexagonal phase rather than the monoclinic phase⁴⁷. In the present study, we have observed the normal trend of transition in the case of Lu_2O_3 and Tm_2O_3 , but contrary to these results, Eu_2O_3 shows a transition from cubic to hexagonal phase, which is due to lower energy of hexagonal phase.

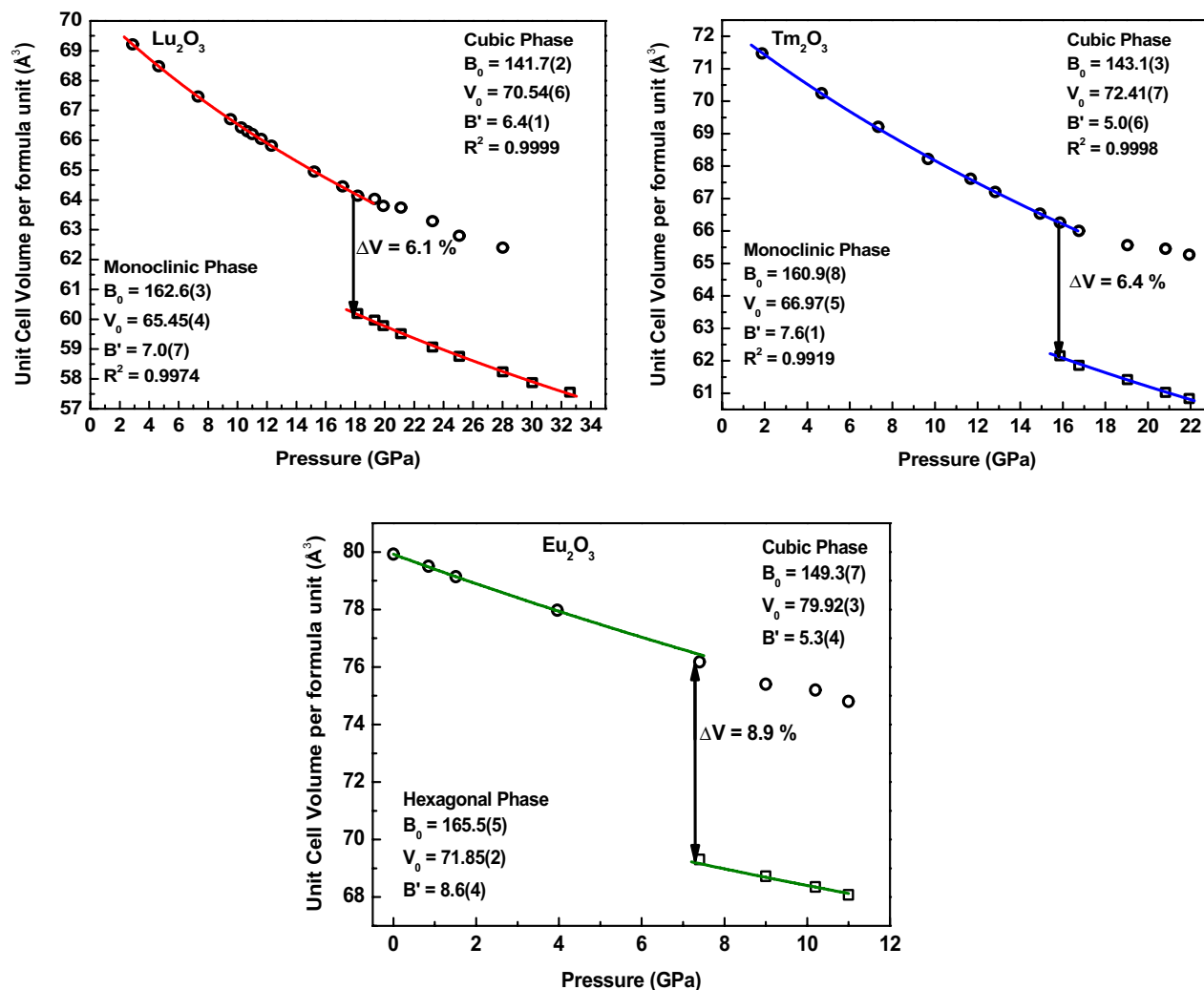


Figure 5. P-V plots for Lu₂O₃, Tm₂O₃ and Eu₂O₃. The symbols represent the experimental data and solid line represents the fit using the BM EOS. Error in the volume is smaller than the symbol size.

Effect of crystallite size on transition pressure

In Lu₂O₃, the structural transition is initiated around the 17.1 GPa of pressure and completed at 30.0 GPa with the disappearance of all the peaks corresponding to the cubic phase. These results are found to be consistent with the transition pressure of 17 GPa, reported by Lin et al. in the crystals of Lu₂O₃²⁹. The value of the transition pressure is also found to be consistent with the our previously reported high pressure Raman spectra of Lu₂O₃ in which the phase is found to be stable up to the pressure of 15 GPa³⁰. However, the pressure at which the transition starts in bulk is 12.7 GPa as reported by Jiang et al., which is lower by a value of 5 GPa as compared to the nanocrystalline Lu₂O₃²⁸.

In case of Tm₂O₃, also, the transition pressure is found to be higher than the theoretically predicted value of 8 GPa. The transition pressure also has a slightly higher value than the pressure reported by Irshad et al.²⁷ for having a crystallite size of 112 nm estimated using the results from the refinement.

In Eu₂O₃, we have observed a new peak at around 7.4 GPa of pressure which is roughly in agreement with our previously reported Raman data in which the phase transition started around 4.79 GPa of pressure²⁵. Although, we cannot exactly compare the starting pressure in the case of XRD data as pressure is increased manually in both cases, however, in both investigations, i.e., Raman and XRD studies, we have observed the transition from cubic to hexagonal phase. It may also be mentioned here that Raman investigations are more sensitive to structural changes and therefore, lattice disturbances prior to shifting to a new phase are more likely to be reflected earlier in the Raman measurements as compared to XRD measurements. Also, these results are in agreement with other researchers, in terms of the observation of the cubic to hexagonal phase transition^{22,23}. Yu et al.²³ reported a phase transition in the nano Eu₂O₃ having crystallite size of 18 nm which is less than our crystallite size and hence higher transition pressure for Eu₂O₃. Further, this observation is also consistent with our observation in case of Lu₂O₃ and Tm₂O₃. It is important to mention here that all the presently obtained results of the HPXRD data agree more or less with our previously reported results of high-pressure Raman investigations reported elsewhere^{25,30}. In all these studies the mixture of methanol:ethanol in the 4:1 is used as the pressure transmitting medium which has a hydrostatic pressure limit of 10.5 GPa³³. As reported, non-hydrostatic pressure may cause deviatoric stresses

Material	Phase		B_0 (GPa)	B_0'	V_0/Z (\AA^3)	Crystallite size
Lu_2O_3	Cubic	This work	141.7 (2)	6.4 (1)	70.54 (6)	30 nm
		Jiang et al. ²⁸	214 (6)	9 (1)	70.06	Bulk
		Lin et al. ²⁹	113.5 (7)	1.7 (3)	–	Pulverized crystals
	Monoclinic	This work	162.6(3)	7.0 (7)	65.45 (4)	30 nm
		Jiang et al. ²⁹	218 (13)	2.3 (3)	65.2 (2)	Bulk
Tm_2O_3	Cubic	This work	143.1 (3)	5.0 (6)	72.41 (7)	35 nm
		Irshad et al. ²⁷	149 (2)	4.8 (5)	72.10	112 nm
		Sahu et al. ²⁶	154.5	4 (fixed)	–	–
	Monoclinic	This work	160.9 (8)	7.6 (1)	66.97 (5)	35 nm
		Irshad et al. ²⁷	169 (2)	4 (fixed)	66.52	112 nm
Eu_2O_3	Cubic	This work	149.3 (7)	5.3(4)	79.92 (3)	66 nm
		Jiang et al. ²²	145 (2)	4 (fixed)	80.30 (3)	Bulk
		Yu et al. ²³	178(5)	4(fixed)	–	18 nm
	Hexagonal	This work	165.5 (5)	8.6 (4)	71.85 (2)	66 nm
		Irshad et al. ³⁵	165 (6)	4 (fixed)	71.35	–
		Jiang et al. ²²	151 (6)	4 (fixed)	74.4 (3)	Bulk
		Yu et al. ²³	229 (2)	4 (fixed)	–	18 nm

Table 2. Values of various parameters obtained from the fitting of the P-V graphs.

and lead to significant broadening above the hydrostatic limit⁴⁸. However, in the present exercise, we did not observe such an increase in the line-widths and therefore, deviatoric stresses, if present, apparently do not play a major role in determining the phase transition. This fact can also be supported by Eu_2O_3 data where the phase transition initiated below the hydrostatic limit.

In present case, the higher value of the transition pressure can be attributed to the smaller crystallite size of 30 nm and 35 nm in Lu and Tm oxides. Several researchers have reported similar behaviour for a number of other REOs^{29,49}. Also, our group has earlier carried out studies on a number of other REOs and observed the higher stability of nanocrystalline materials^{43–45,50–52}. It is therefore implied that the crystallite size plays a role in the transition paths and well as high pressure phases assumed by the nano-REOs. The higher stability of the Lu and Tm oxide nanomaterials can be attributed to the fact that polymorphic transition is part of solid–solid phase transformation where the nucleation usually occurs at the defect site in the lattice. However, in case of the nanocrystalline materials the defect density is limited due to which we need to overpressure the system to induce a phase transition. This over pressuring of the system explains the higher transition pressure in case of the smaller nanocrystalline materials. These observations are also consistent with the lower transition pressure observed for Eu_2O_3 with a larger crystallite size of 66 nm.

It is also worth mentioning that, as the number of f-electrons increase, the ionic radii of the lanthanides decreases which is also known as the lanthanide contraction. And due to this contraction, the stability of structure increases and as a result higher pressure is needed to change the structure. In our case, Eu has the highest ionic radius followed by Tm and then Lu, which suggests a lower transition pressure for Eu and highest for Lu. This agrees very well with our experimental results. This also agrees with our previously reported results for other REOs wherein the transition pressure was found to increase with decrease in the ionic radii⁵³.

Hence, from the above discussion, the transition trend in the REOs remains the same; however, if we compare the onset pressure and pressure at which transition is completed, the values for nanocrystalline materials are higher than their bulk counterparts. Therefore, it may be surmised that transition pressure has an inverse relationship with the crystallite size. As mentioned, in all the presently investigated nanocrystalline materials, we have observed a change in the transition pressure as compared to their reported bulk counterparts and observed that smaller nanocrystalline materials show higher stability as compared to bulk materials^{23,25–28,44,46,51,54–57} and hence higher transition pressure.

A comparison of the reported data is shown graphically in Fig. 6, along with the data of various other oxides. It is evident from the figure that bulk materials have the lowest transition pressure in comparison to their microstructured and nanocrystalline materials. Also, it is important to mention that nanomaterials having lower crystallite size show higher transition pressure.

Effect of nanocrystalline nature of materials on bulk modulus

However, the results of the bulk modulus for the nanocrystalline materials are not as straightforward. It is found that the value of the bulk modulus for nanocrystalline materials is found to be lower than their bulk counterpart for some materials^{40,49}, and contrary to this, it is found to be higher for some^{23,56,57}. Some other oxides such as In_2O_3 ⁵⁸, Al_2O_3 ⁵⁹, TiO_2 ⁶⁰, SnO_2 ⁶¹ also show a decrease in the bulk modulus with the decrease in the crystallite size.

As mentioned, the competition between the larger surface area and limited density of storage defects can play an important role in deciding compressibility of the materials. Due to the limited density of this defect storage, most of the nanoparticles (size less than the critical size (10–30 nm)) are defect free and hence show greater stability with external stimuli and perturbations and demonstrate higher compressibility which in turn

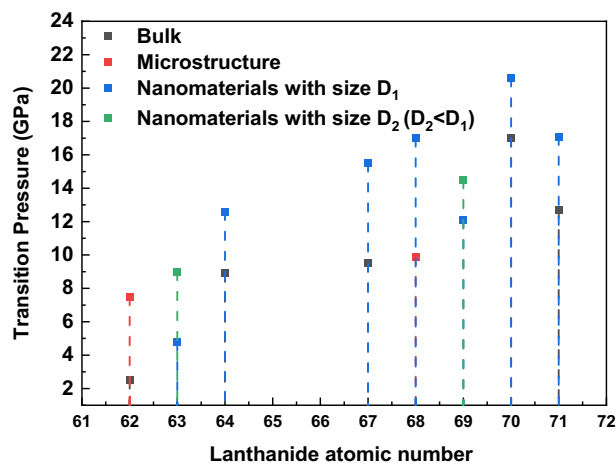


Figure 6. Transition pressure dependence on the crystallite size for various rare earth oxides^{23,25–28,45,47,51,54–57}.

leads to the lower value of the bulk modulus⁴⁹. As discussed earlier, the higher value of transition pressure can be attributed to the fact that the phase transitions usually start from the defective region.

On the contrary, Yu et al. reported a higher value of the bulk modulus for the nanocrystalline Eu_2O_3 having crystallite size of 18 nm calculated using the Debye Scherrer equation in comparison to the bulk Eu_2O_3 ²³.

Jiang et al. found the value of bulk modulus of Sm_2O_3 to be 149 GPa, when B_0' is fixed at 4⁶². However, for the submicron Sm_2O_3 procured from Acros, Guo et al. reported lesser value of the bulk modulus i.e., 142 GPa⁴⁰. Yan et al. calculated the bulk modulus for the nano crystalline Ho_2O_3 having crystallite size of 14 nm estimated using Debye-Scherrer equation, which was 10 % lower than their bulk counterpart⁴⁹. It is worth mentioning here that the higher value of compressibility of nano crystals is due to the surface effects. As the size increases, the contribution of these surface effects decreases, leading to lower compressibility and hence higher bulk modulus. In case of micron size structure e.g., for crystallite size in micrometre for Er_2O_3 , Guo et al. reported a value of 200 GPa and 8.4 for the bulk modulus and first derivative of the bulk modulus respectively⁵⁷. On the other hand, for the nanocrystalline Er_2O_3 the value for the B_0 and B' is found to be 181 and 4.07 respectively by Ren et al. which is less than submicron Er_2O_3 ⁵⁶.

Our results are consistent with these results as the value of bulk modulus for the nanomaterials is lower than those reported for the bulk materials for Lu_2O_3 and Tm_2O_3 . However, in case of Lu_2O_3 , Lin et al. have reported the values which are lower than our values which can be due to the fact that the pulverized crystal has been used for the present studies²⁹. In case of Tm_2O_3 , results by the Irshad et al. are only slightly higher than the reported values which is expected as the study was carried out on the material having a crystallite size of 112 nm²⁷.

It has been reported that with an increase in the atomic number, the value of the bulk modulus increases for the bulk REOs²⁶. However, our present results neither endorse nor refute this statement since the bulk modulus values for the starting cubic phases, although marginally higher for Eu_2O_3 with larger crystallite size, were found comparable when considering the errors mentioned in the parenthesis. In addition, the values may not be directly compared considering the difference in the nano-size of the samples under investigation.

Conclusions

The present investigations show that smaller nanocrystalline REOs show higher stability as compared to their bulk counterparts as well as larger nano-crystallites. The nano-size profoundly affects the transition pressures as well as the bulk modulus. We observed structural phase transitions in nanocrystalline Lu_2O_3 , Tm_2O_3 and Eu_2O_3 under the application of pressure. Transition from cubic to monoclinic phase has been observed for Lu_2O_3 and Tm_2O_3 , whereas transition from cubic to hexagonal phase has been observed for Eu_2O_3 due to lower energy of hexagonal phase. The results obtained using high-energy synchrotron XRD studies are consistent with previously reported high-pressure Raman results. The bulk modulus for all the nanocrystalline REOs have been reported which have values lower than their bulk counterparts.

Data availability

The datasets generated and/or analysed during the current study are available in the COD repository, <https://www.crystallography.net/cod/result.php>.

Received: 27 February 2023; Accepted: 6 September 2023

Published online: 13 October 2023

References

- Shen, Y. et al. A universal multifunctional rare earth oxide coating to stabilize high-voltage lithium layered oxide cathodes. *Energy Storage Mater.* **56**, 155–164. <https://doi.org/10.1016/j.ensm.2023.01.015> (2023).

2. Hossain, M. K. *et al.* A review on recent applications and future prospects of rare earth oxides in corrosion and thermal barrier coatings, catalysts, tribological, and environmental sectors. *Ceram. Int.* **48**, 32588–32612. <https://doi.org/10.1016/j.ceramint.2022.07.220> (2022).
3. Stamenković, T. *et al.* Characterization and photocatalytic application of SrGd₂O₄ doped with rare earth Sm³⁺ and Dy³⁺ ions. *Surf. Interfaces* **37**, 102755. <https://doi.org/10.1016/j.surf.2023.102755> (2023).
4. Taşgin, Y., Pekdemir, M. E., Yılmaz, M., Kanca, M. S. & Kök, M. Physical and shielding properties of Er₂O₃ rare earth oxide compound content on PCL/PEG blend. *Polym. Bull.* <https://doi.org/10.1007/s00289-023-04818-1> (2023).
5. Eguchi, K. Ceramic materials containing rare earth oxides for solid oxide fuel cell. *J. Alloys Compd.* **250**(1–2), 486–491. [https://doi.org/10.1016/S0925-8388\(96\)02629-1](https://doi.org/10.1016/S0925-8388(96)02629-1) (1997).
6. Alharshan, G. A. *et al.* Radiation shielding capacity of Li₂O–SiO₂/GeO₂ glasses doped with rare earth oxides: Nuclear security applications. *Radiat. Phys. Chem.* <https://doi.org/10.1016/j.radphyschem.2022.110703> (2023).
7. Lian, X. *et al.* Design and mechanical properties of SiC reinforced Gd₂O₃/6061Al neutron shielding composites. *Ceram. Int.* <https://doi.org/10.1016/j.ceramint.2023.04.092> (2023).
8. Fornasiero, L., Mix, E., Peters, V., Petermann, K. & Huber, G. New oxide crystals for solid state lasers. *Cryst. Res. Technol.* **34**(2), 255–260. [https://doi.org/10.1002/\(SICI\)1521-4079\(199902\)34:2%3c255::AID-CRAT255%3e3.0.CO;2-U](https://doi.org/10.1002/(SICI)1521-4079(199902)34:2%3c255::AID-CRAT255%3e3.0.CO;2-U) (1999).
9. Bulus, I. *et al.* Europium-doped boro-telluro-dolomite glasses for red laser applications: Basic insight into spectroscopic traits. *J. Non Cryst. Solids* **534**, 119949. <https://doi.org/10.1016/j.jnoncrysol.2020.119949> (2020).
10. Hossain, M. K. *et al.* Current applications and future potential of rare earth oxides in sustainable nuclear, radiation, and energy devices: A review. *ACS Appl. Electron. Mater.* **4**(7), 3327–3353. <https://doi.org/10.1021/acsaem.2c00069> (2022).
11. Lee, J. *et al.* Improvement of oxide chemical mechanical polishing performance by increasing Ce³⁺/Ce⁴⁺ ratio in ceria slurry via hydrogen reduction. *Mater. Sci. Semicond. Process* <https://doi.org/10.1016/j.mssp.2023.107349> (2023).
12. Sabia, R. & Stevens, H. J. Performance characterization of cerium oxide abrasives for chemical-mechanical polishing of glass. *Mach. Sci. Technol.* **4**(2), 235–251. <https://doi.org/10.1080/10940340008945708> (2000).
13. Bedekar, V. *et al.* Rare-earth doped gadolinia based phosphors for potential multicolor and white light emitting deep UV LEDs. *Nanotechnology* **20**(12), 125707. <https://doi.org/10.1088/0957-4484/20/12/125707> (2009).
14. Nosov, V. I., Ponomarev-Stepnoi, N. N., Portnoi, K. I. & Savelev, E. G. *Dispersion-Type Absorber Materials for Thermal Reactor Control Rods** (PergammPressLtd, 1965).
15. Alzahrani, J. S. *et al.* Optical properties and radiation shielding performance of tellurite glassy composites: Role of rare earth oxides. *Radiat. Phys. Chem.* **212**, 111168. <https://doi.org/10.1016/j.radphyschem.2023.111168> (2023).
16. Turşucu, A., Elmahroug, Y. & Yılmaz, D. Radiation shielding calculations of some selected rare earth oxides. *Radiat. Phys. Chem.* <https://doi.org/10.1016/j.radphyschem.2023.111066> (2023).
17. Dedov, A. G. *et al.* Oxidative coupling of methane catalyzed by rare earth oxides: Unexpected synergistic effect of the oxide mixtures. *Appl. Catal. A Gen.* **245**(2), 209–220. [https://doi.org/10.1016/S0926-860X\(02\)00641-5](https://doi.org/10.1016/S0926-860X(02)00641-5) (2003).
18. Muthulakshmi, V., Balaji, M. & Sundrarajan, M. Biomedical applications of ionic liquid mediated samarium oxide nanoparticles by *Andrographis Paniculata* leaves extract. *Mater. Chem. Phys.* <https://doi.org/10.1016/j.matchemphys.2019.122483> (2019).
19. Jairam, L. S. *et al.* A review on biomedical and dental applications of cerium oxide nanoparticles—Unearthing the potential of this rare earth metal. *J. Rare Earths* <https://doi.org/10.1016/j.jre.2023.04.009> (2023).
20. Singh, J. *et al.* Optical and electro-catalytic studies of nanostructured thulium oxide for vitamin C detection. *J. Alloys Compd.* **578**, 405–412. <https://doi.org/10.1016/j.jallcom.2013.06.026> (2013).
21. Hoekstra, R. Phase relationships in rare earth sesquioxides at high pressure. *Inorg. Chem.* **5**(5), 754–757 (1965).
22. Sheng, J. *et al.* The phase transition of Eu₂O₃ under high pressures. *Chin. Phys. Lett.* **26**(7), 076101. <https://doi.org/10.1088/0256-307X/26/7/076101> (2009).
23. Yu, Z., Wang, Q., Ma, Y. & Wang, L. X-ray diffraction and spectroscopy study of nano-Eu₂O₃ structural transformation under high pressure. *J. Alloys Compd.* **701**, 542–548. <https://doi.org/10.1016/j.jallcom.2017.01.143> (2017).
24. Dilawar, N. *et al.* Structural transition in nanostructured Eu₂O₃ under high pressures. *J. Nanosci. Nanotechnol.* **6**, 105–113 (2006).
25. Bura, N., Yadav, D., Bhorriya, A., Singh, J. & Dilawar Sharma, N. Influence of varying thermodynamic parameters on the structural behavior of nano-crystalline europium sesquioxide. *J. Alloys Compd.* **856**, 158129. <https://doi.org/10.1016/j.jallcom.2020.158129> (2021).
26. Sahu, P. C., Lonappan, D. & Shekar, N. V. C. High pressure structural studies on rare-earth sesquioxides. *J. Phys. Conf. Ser.* **377**, 012015. <https://doi.org/10.1088/1742-6596/377/1/012015> (2012).
27. Irshad, K. A. *et al.* Pressure induced structural phase transition in rare earth sesquioxide Tm₂O₃: Experiment and ab initio calculations. *J. Appl. Phys.* **124**, 155901. <https://doi.org/10.1063/1.5049223> (2018).
28. Jiang, S. *et al.* Pressure-induced phase transition in cubic Lu₂O₃. *J. Appl. Phys.* <https://doi.org/10.1063/1.3499301> (2010).
29. Lin, C. M. *et al.* Phase transitions in Lu₂O₃ under high pressure. *Solid State Commun.* **150**(33–34), 1564–1569. <https://doi.org/10.1016/j.ssc.2010.05.046> (2010).
30. Bura, N., Yadav, D., Singh, J. & Sharma, N. D. Phonon variations in nano-crystalline lutetium sesquioxide under the influence of varying temperature and pressure. *J. Appl. Phys.* **126**, 245901. <https://doi.org/10.1063/1.5125702> (2019).
31. Ren, X. *et al.* Anomalous pressure-induced phase transformation in nano-crystalline erbium sesquioxide (Er₂O₃): Partial amorphization under compression. *High Press Res.* **34**(1), 70–77. <https://doi.org/10.1080/08957959.2013.867039> (2014).
32. Liu, B. *et al.* High-pressure Raman study on CeO₂ nanospheres self-assembled by 5nm CeO₂ nanoparticles. *Phys. Status Solidi B Basic Res.* **248**(5), 1154–1157. <https://doi.org/10.1002/pssb.201000807> (2011).
33. Klotz, S., Chervin, J. C., Munsch, P. & Le Marchand, G. Hydrostatic limits of 11 pressure transmitting media. *J. Phys. D Appl. Phys.* **42**(7), 075413. <https://doi.org/10.1088/0022-3727/42/7/075413> (2009).
34. Bura, N., Bhorriya, A., Yadav, D., Singh, J. & Dilawar Sharma, N. Temperature-dependent phonon behavior in nanocrystalline Tm₂O₃: Fano interference and phonon anharmonicity. *J. Phys. Chem. C* **125**(33), 18259–18269. <https://doi.org/10.1021/acs.jpcc.1c04250> (2021).
35. Irshad, K. A. & Chandra Shekar, N. V. Anomalous lattice compressibility of hexagonal Eu₂O₃. *Mater. Chem. Phys.* **195**, 88–93. <https://doi.org/10.1016/j.matchemphys.2017.04.012> (2017).
36. Ren, X., Yan, X., Yu, Z., Li, W. & Wang, L. Photoluminescence and phase transition in Er₂O₃ under high pressure. *J. Alloys Compd.* **725**, 941–945. <https://doi.org/10.1016/j.jallcom.2017.07.219> (2017).
37. Jiang, S. *et al.* Phase transformation of Ho₂O₃ at high pressure. *J. Appl. Phys.* **110**(1), 2–7. <https://doi.org/10.1063/1.3603027> (2011).
38. Jiang, S. *et al.* Structural transformations in cubic Dy₂O₃ at high pressures. *Solid State Commun.* **169**, 37–41. <https://doi.org/10.1016/j.ssc.2013.06.027> (2013).
39. Bai, L. *et al.* Pressure-induced phase transformations in cubic Gd₂O₃. *J. Appl. Phys.* **106**(7), 1–5. <https://doi.org/10.1063/1.3236580> (2009).
40. Guo, Q., Zhao, Y., Jiang, C., Mao, W. L. & Wang, Z. Phase transformation in Sm₂O₃ at high pressure: In situ synchrotron X-ray diffraction study and ab initio DFT calculation. *Solid State Commun.* **145**(5–6), 250–254. <https://doi.org/10.1016/j.ssc.2007.11.019> (2008).
41. Lonappan, D. *et al.* Cubic to hexagonal structural transformation in Gd₂O₃ at high pressure. *Philos. Mag. Lett.* **88**(7), 473–479. <https://doi.org/10.1080/09500830802232534> (2008).

42. Zhang, F. X., Lang, M., Wang, J. W., Becker, U. & Ewing, R. C. Structural phase transitions of cubic Gd₂O₃ at high pressures. *Phys. Rev. B Condens. Matter Mater. Phys.* **78**(6), 1–9. <https://doi.org/10.1103/PhysRevB.78.064114> (2008).
43. Dilawar Sharma, N. *et al.* Pressure-induced structural transition trends in nanocrystalline rare-earth sesquioxides: A Raman investigation. *J. Phys. Chem. C* **120**(21), 11679–11689. <https://doi.org/10.1021/acs.jpcc.6b02104> (2016).
44. Pandey, S. D., Samanta, K., Singh, J., Sharma, N. D. & Bandyopadhyay, A. K. Anharmonic behavior and structural phase transition in Yb₂O₃. *AIP Adv.* <https://doi.org/10.1063/1.4858421> (2013).
45. Sharma, N. D. *et al.* Pressure-induced anomalous phase transformation in nano-crystalline dysprosium sesquioxide. *J. Raman Spectrosc.* **42**(3), 438–444. <https://doi.org/10.1002/jrs.2720> (2011).
46. Dilawar, N. *et al.* Anomalous high pressure behaviour in nanosized rare earth sesquioxides. *Nanotechnology* **19**(11), 115703. <https://doi.org/10.1088/0957-4484/19/11/115703> (2008).
47. Richard, D., Errico, L. A. & Rentería, M. Structural, electronic and hyperfine properties on Sm₂O₃, Eu₂O₃ and Gd₂O₃ phases. *Comput. Condens. Matter* **16**, e00327. <https://doi.org/10.1016/j.cocom.2018.e00327> (2018).
48. Errandonea, D., Muñoz, A. & Gonzalez-Platas, J. Comment on ‘High-pressure x-ray diffraction study of YBO₃/Eu₃₊, GdBO₃, and EuBO₃: Pressure-induced amorphization in GdBO₃’. *J. Appl. Phys.* **115**, 216101 (2014).
49. Yan, X., Ren, X., He, D., Chen, B. & Yang, W. Mechanical behaviors and phase transition of Ho₂O₃ nanocrystals under high pressure. *J. Appl. Phys.* **116**(3), 1–5. <https://doi.org/10.1063/1.4890341> (2014).
50. Dogra, S. *et al.* High pressure behavior of nano-crystalline CeO₂ up to 35 GPa: A Raman investigation. *High Press. Res.* **31**(2), 292–303. <https://doi.org/10.1080/08957959.2011.576674> (2011).
51. Pandey, S. D., Samanta, K., Singh, J., Sharma, N. D. & Bandyopadhyay, A. K. Raman scattering of rare earth sesquioxide Ho₂O₃: A pressure and temperature dependent study. *J. Appl. Phys.* **116**(13), 1–8. <https://doi.org/10.1063/1.4896832> (2014).
52. Dogra, S. *et al.* Phase progression via phonon modes in lanthanide dioxides under pressure. *Vib. Spectrosc.* **70**, 193–199. <https://doi.org/10.1016/j.vibspec.2013.12.005> (2014).
53. N. and Dilawar Sharma and A. K.; Bandyopadhyay, “Chapter 12 “Raman Spectroscopic Studies of the Rare Earth Sesquioxides and Related Compounds under High Pressures,” in *Rare Earths: New Research*, Z. Liu, Ed., Nova Science publishers.
54. J. P. McClure, High pressure phase transitions in lanthanide oxides.
55. Dilawar Sharma, N., Singh, J., Vijay, A., Samanta, K. & Dogra Pandey, S. Investigations of anharmonic effects via phonon mode variations in nanocrystalline Dy₂O₃, Gd₂O₃ and Y₂O₃. *J. Raman Spectrosc.* **48**(6), 822–828. <https://doi.org/10.1002/jrs.5120> (2017).
56. Ren, X., Yan, X., Yu, Z., Li, W. & Yang, K. Size-dependent phase transition of Er₂O₃ under high pressure. *Appl. Phys. Lett.* **112**, 143102 (2018).
57. Guo, Q. *et al.* Pressure-induced cubic to monoclinic phase transformation in erbium sesquioxide Er₂O₃. *Inorg. Chem.* **46**(15), 6164–6169. <https://doi.org/10.1021/ic070154g> (2007).
58. Sans, J. A. *et al.* Structural and vibrational properties of corundum-type In₂O₃ nanocrystals under compression. *Nanotechnology* **28**, 205701. <https://doi.org/10.1088/1361-6528/aa6a3f> (2017).
59. Chen, B., Penwell, D., Benedetti, L. R., Jeanloz, R. & Kruger, M. B. Particle-size effect on the compressibility of nanocrystalline alumina. *Phys. Rev. B Condens. Matter Mater. Phys.* **66**(14), 1–4. <https://doi.org/10.1103/PhysRevB.66.144101> (2002).
60. Al-Khatatbeh, Y., Lee, K. K. M. & Kiefer, B. Compressibility of nanocrystalline TiO₂ anatase. *J. Phys. Chem. C* **116**(40), 21635–21639. <https://doi.org/10.1021/jp3075699> (2012).
61. He, Y. *et al.* High-pressure behavior of SnO₂ nanocrystals. *Phys. Rev. B Condens. Matter Mater. Phys.* **72**(21), 8–11. <https://doi.org/10.1103/PhysRevB.72.212102> (2005).
62. Jiang, S., Liu, J., Lin, C., Li, X. & Li, Y. High-pressure x-ray diffraction and Raman spectroscopy of phase transitions in Sm₂O₃. *J. Appl. Phys.* **113**(11), 1–7. <https://doi.org/10.1063/1.4795504> (2013).

Acknowledgements

The authors are grateful to Director, CSIR-NPL for constant encouragement and to Council of Scientific and Industrial Research (CSIR) as well as University Grants Commission (UGC) for providing research fellowships under the grant numbers 19/06/2016(i)EU-V, 18/06/2017(i)EU-V and 1448| (CSIR- UGC NET DEC. 2017) respectively.

Author contributions

N.B. carried out the preliminary investigations and wrote the manuscript. A.B. and D.Y. helped during the experiments. V.S. supervised the experiments. J.S. and B.G. helped in the analysis of the data. H.K.P. and N.D. edited the manuscript and supervised. All the authors reviewed the manuscript.

Competing interests

The authors declare no competing interests.

Additional information

Supplementary Information The online version contains supplementary material available at <https://doi.org/10.1038/s41598-023-42181-3>.

Correspondence and requests for materials should be addressed to N.D.S.

Reprints and permissions information is available at www.nature.com/reprints.

Publisher’s note Springer Nature remains neutral with regard to jurisdictional claims in published maps and institutional affiliations.



Open Access This article is licensed under a Creative Commons Attribution 4.0 International License, which permits use, sharing, adaptation, distribution and reproduction in any medium or format, as long as you give appropriate credit to the original author(s) and the source, provide a link to the Creative Commons licence, and indicate if changes were made. The images or other third party material in this article are included in the article's Creative Commons licence, unless indicated otherwise in a credit line to the material. If material is not included in the article's Creative Commons licence and your intended use is not permitted by statutory regulation or exceeds the permitted use, you will need to obtain permission directly from the copyright holder. To view a copy of this licence, visit <http://creativecommons.org/licenses/by/4.0/>.

© The Author(s) 2023